applied optics

Freeform three-mirror anastigmatic large-aperture telescope and receiver optics for CMB-S4

Patricio A. Gallardo,[1,*] Roberto Puddu,[2] Kathleen Harrington,[3,4] Bradford Benson,[1,4,5] John E. Carlstrom,[1,3,4,6,7] Simon R. Dicker,[8] Nick Emerson,[9] Jon E. Gudmundsson,[10,11] Michele Limon,[8] Jeff McMahon,[1,4,5,6,7] Johanna M. Nagy,[12] Tyler Natoli,[1,4] Michael D. Niemack,[13,14] Stephen Padin,[15] John Ruhl,[12] Sara M. Simon,[5] and the CMB-S4 Collaboration[†]

[1]*Kavli Institute for Cosmological Physics, University of Chicago, Chicago, Illinois 60637, USA*
[2]*Instituto de Astrofísica and Centro de Astro-Ingeniería, Facultad de Física, Pontificia Universidad Católica de Chile, Santiago, Chile*
[3]*High Energy Physics Division, Argonne National Laboratory, Argonne, Illinois 60439, USA*
[4]*Department of Astronomy and Astrophysics, University of Chicago, Chicago, Illinois 60637, USA*
[5]*Fermi National Accelerator Laboratory, Batavia, Illinois 60510, USA*
[6]*Department of Physics, University of Chicago, Chicago, Illinois 60637, USA*
[7]*Enrico Fermi Institute, University of Chicago, Chicago, Illinois 60637, USA*
[8]*Department of Physics and Astronomy, University of Pennsylvania, Philadelphia, Pennsylvania 19104, USA*
[9]*Steward Observatory, The University of Arizona, Tucson, Arizona 85721, USA*
[10]*The Oskar Klein Centre, Department of Physics, Stockholm University, Stockholm, Sweden*
[11]*Science Institute, University of Iceland, 107 Reykjavik, Iceland*
[12]*Physics Department, Case Western Reserve University, Cleveland, Ohio 44106, USA*
[13]*Department of Physics, Cornell University, Ithaca, New York 14850, USA*
[14]*Department of Astronomy, Cornell University, Ithaca, New York 14850, USA*
[15]*California Institute of Technology, Pasadena, California 91125, USA*
[†]*https://cmb-s4.org/team/*
*pgallardo@uchicago.edu

CMB-S4, the next-generation ground-based cosmic microwave background (CMB) observatory, will provide detailed maps of the CMB at millimeter wavelengths to dramatically advance our understanding of the origin and evolution of the universe. CMB-S4 will deploy large- and small-aperture telescopes with hundreds of thousands of detectors to observe the CMB at arcminute and degree resolutions at millimeter wavelengths. Inflationary science benefits from a deep delensing survey at arcminute resolutions capable of observing a large field of view at millimeter wavelengths. This kind of survey acts as a complement to a degree angular resolution survey. The delensing survey requires a nearly uniform distribution of cameras per frequency band across the focal plane. We present a large-throughput (9.4° field of view), large-aperture (5-m diameter) freeform three-mirror anastigmatic telescope and an array of 85 cameras for CMB observations at arcminute resolutions, which meets the needs of the delensing survey of CMB-S4. A detailed prescription of this three-mirror telescope and cameras is provided, with a series of numerical calculations that indicates expected optical performance and mechanical tolerance. © 2024 Optica Publishing Group

1. INTRODUCTION

Advances in sensitivity of cosmic microwave background (CMB) observatories in the last decades and the rich science that benefits from these observations have motivated the need for a large-scale CMB survey capable of delivering low-noise maps of the cosmic microwave background at arcminute and degree angular scales, such as CMB-S4. The CMB-S4 science goals are broad; they include the search for primordial gravitational waves (a signature of early inflation), constraining dark energy, determining the role of light relic particles in the structure and history of the universe, tests of gravity at very large scales, measurements of the emergence of clusters of galaxies, time-domain observations of transients at millimeter-wavelengths and even the exploration of our Solar System. The non-inflationary science

goals of CMB-S4 drive the need for wide, arcminute-resolution observations of the millimeter-wave sky, while the inflationary science goal drives the need for a deep, degree-resolution survey. The inflation science goal also benefits from arcminute observations, which enable corrections of the B-mode signal in a processing step often referred to as delensing. Furthermore, the deep delensing survey benefits from a wide field of view with hundreds of thousands of detectors giving uniform frequency coverage on overlapping patches of sky [1,2].

Diffraction-limited large-aperture (6-m class) telescopes are able to achieve arcminute angular resolution observations of the CMB at millimeter wavelengths. Next-generation high-sensitivity CMB observations require a large field of view to accommodate hundreds of thousands of detectors with minimal systematics. Unobstructed optical configurations provide low optical systematics, for which off-axis configurations have been used in many large-aperture CMB telescopes. In the past, off-axis Gregorian telescopes (where light focuses between the primary and secondary mirrors) [3,4] provided fields of view large enough to accommodate multiple cameras. Later the crossed Dragone configuration has been used [5] to accommodate a larger focal plane with minimal cross polarization, satisfying the Mizuguchi–Dragone condition [6,7], and the use of small corrections to the mirror shapes to minimize aberrations as outlined in [8]. Advances in technology have enabled the construction of receivers containing increasing numbers of detectors, which are currently accommodated in crossed Dragone telescopes. The crossed Dragone configuration however produces rapidly changing astigmatism, which is hard to correct even with high-order aspheric terms.

In the past, 6-m class telescope mirrors have been manufactured by machining aluminum panels and carefully aligning them to form a large dish. Even with careful alignment, this approach leads to complex diffraction patterns from the small gaps between panels that spill power to large angular scales on the sky. These characteristics (astigmatism-related field of view limitations at 1.1 mm and panel gap diffraction) motivate the exploration of new technological solutions such as the incorporation of a third mirror, the use of freeform surfaces and the implementation of seamless mirrors to improve performance in order to achieve the levels of sensitivity, wide field of view, uniform band coverage and low-diffraction sidelobes required in the next generation of CMB experiments (see Fig. 1).

Three-mirror telescopes are able to cancel all first-order aberrations (including astigmatism), achieving a large field of view with diffraction-limited performance. Notable three-mirror telescopes include JWST, the Gaia satellite and future astronomical observatories such as the Vera C. Rubin Observatory or the E-ELT [9–12]. Most optical and infrared telescopes are obstructed by their secondary mirror and its supporting structure, which introduces beam asymmetries. An unobstructed off-axis three-mirror telescope design concept for CMB observations has been proposed [13] with standard surfaces (described by a radius of curvature, and a conic constant). This telescope concept has been designed to be manufacturable with 5-m monolithic mirrors. Monolithic mirrors provide an attractive balance between manufacturability and a low level of large-angle diffraction. In this paper we explore such a three-mirror telescope and provide an updated design. This telescope
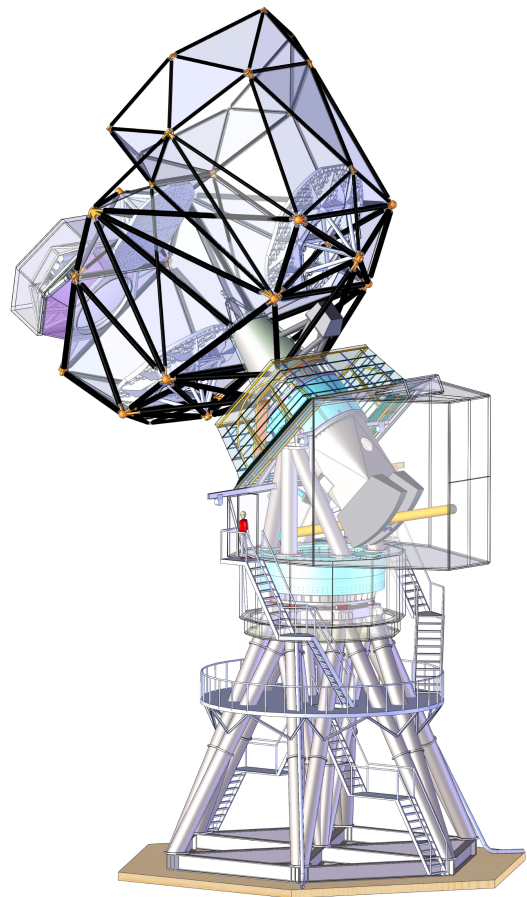

Fig. 1. Rendering of the three-mirror anastigmatic concept for the South Pole CMB-S4 large-aperture telescope.

design has 9.4° of field of view with excellent image quality at $\lambda = 1.1$ mm and a lower f-number, which allows the same camera concept to be used as for the crossed Dragone design. This facilitates the cryomechanical design and minimizes development complexity. We provide an updated design for a set of 85 cameras (following up on previous work [14]) that populate the focal plane and show expected performance.

This paper is part of a series of development studies to evaluate performance for the South Pole three-mirror large-aperture telescope for CMB-S4 including sidelobes performance [15] and seamless mirror manufacture [16]. This work presents a three-mirror polynomially defined freeform large-aperture (5-m) telescope and 85 three-lens cameras for CMB observations (see Fig. 1). This telescope design evolved from the three-mirror system presented in Padin [13] (herein P18) with a lower f-number ($f/2.6$ versus $f/3.7$) and it was optimized taking into account manufacturability constraints. The three-lens camera design is based on heritage technology from previous CMB experiments [4,17–25], which minimizes engineering risks. The array of 85 cameras can be built using only two optical prescriptions for three silicon lenses as it was briefly described in [14]. This telescope design concept and its array of cameras is intended to be deployed as the South Pole large-aperture telescope for CMB-S4, a large-scale CMB observatory, which will provide maps of the cosmic microwave background with unprecedented levels of sensitivity and wide area coverage.

This paper is structured as follows: Section 1 gives a summary of the state of the art in large-aperture telescopes for CMB bands and summarizes the aim of this study. In Section 2 we give a detailed description of the optics of the updated three-mirror anastigmatic telescope. Section 3 presents the nominal performance for the three-mirror system. Section 4 shows a tolerance analysis of this three-mirror system. Section 5 describes the design of the array of cameras for the telescope. Section 6 describes the performance of the camera system in conjunction with the three-mirror telescope optics. Section 7 contains a tolerancing analysis for one single camera of the array, in conjunction with the three-mirror system. We conclude in Section 8.

2. TELESCOPE DESIGN DESCRIPTION

A previous optical design of a three-mirror telescope for CMB observations proposed an off-axis configuration where the tertiary is approximately the same size as the primary. The size of the tertiary is driven by the cancellation of astigmatism over a wide field of view, which can be as large as 9° at 1.1 mm in this configuration. A system with these characteristics has been demonstrated in P18, which follows work in three-mirror telescopes for on-axis configurations [26].

The design presented in P18 used a concave primary mirror, a convex secondary and a concave tertiary. In the updated design, we maintain this optical configuration to allow compatibility with existing mechanical engineering development, and we modify the design to yield a lower f-number ($f/2.6$ versus $f/3.7$), which enables a smaller and lighter instrument, illuminated with high Strehl ratios at wavelengths as short as 1.1 mm. This lower f-number is well-matched to the existing crossed Dragone design to be used in the CMB-S4 large-aperture telescopes planned to be deployed in Chile, which are also $f/2.6$ systems [5]. This lower f-number results in a tertiary mirror that is closer to the focal plane. In this design the primary and tertiary mirrors are of comparable size and within manufacturability constraints given by mechanical engineering considerations. Figure 2 (top) shows the optical layout of this updated design.

The three reflective surfaces of the updated three-mirror telescope design are defined with two-dimensional freeform polynomial surfaces in rectangular coordinates. For each mirror, a local coordinate system is defined by translating the origin and rotating the coordinate system around the x-axis. The polynomially defined surface for each mirror is given by

$$z(x, y) = \sum_{i,j}^{i,j \in 0.5} A_{i,j}(x/R)^i (y/R)^j, \qquad \textbf{(1)}$$

where $A_{i,j}$ is the coefficient for the term $x^i y^j$ and R is a normalization radius (equal to 2500 mm). This parametrization has the property of normalizing the x and y coordinates, such that the coefficient $A_{i,j}$ is the magnitude of the sag (the deviation from flat) of the $x^i y^j$ polynomial term. Table 1 shows the coefficients that describe the mirror surfaces for the three mirrors, which depart 15, 47 and 136 mm from a symmetric best-fit conic surface for mirrors M1, M2 and M3, respectively. Rotation angles and locations for the local coordinate systems are shown in Table 2. This telescope design yields a moderately
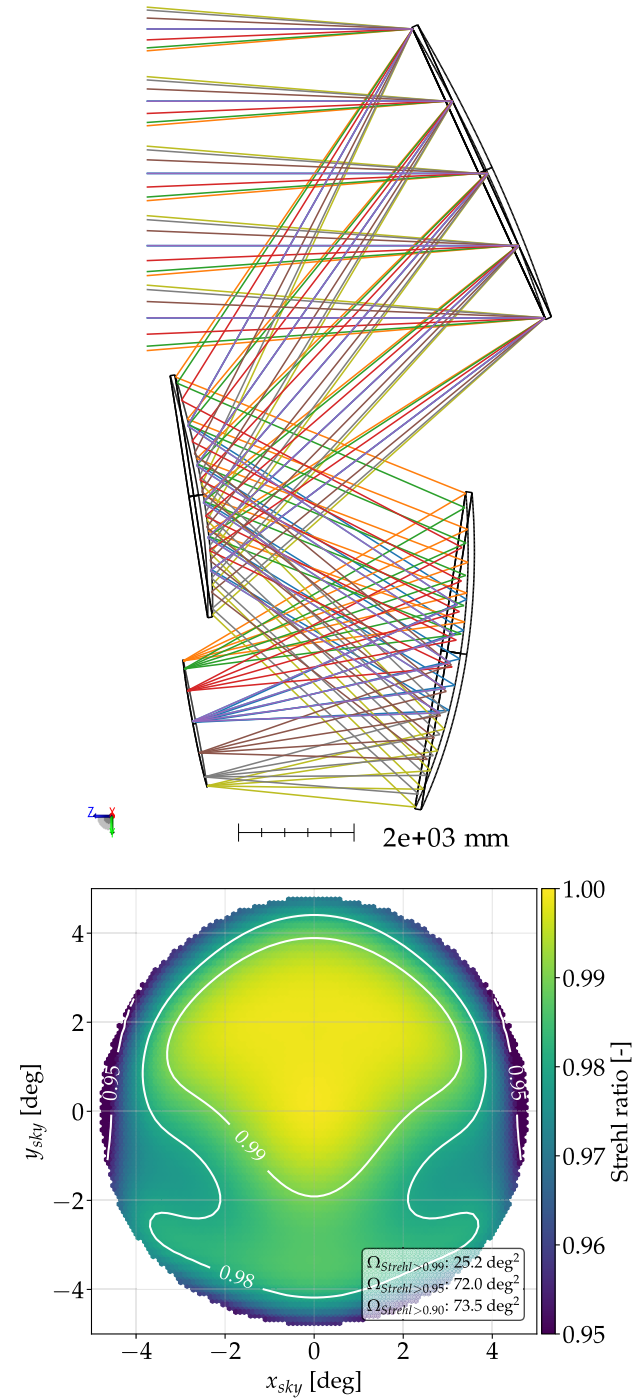

Fig. 2. Top: optical layout of the three-mirror anastigmatic telescope (TMA). Colored rays show extreme fields 4.7° from the boresight. Bottom: unvignetted Strehl ratios at 1.1 mm for a focal plane of 1.1 m in radius and a field of view of 4.7° in semi-diameter. The field of view in this system is limited by vignetting given by the size of the tertiary. Contours and solid angle are shown for Strehls of 0.99, 0.98 and 0.95.

curved focal plane that departs from a plane a maximum of 55 mm (20 mm) over 1.1 m in the $x(y)$ direction. This field curvature can be corrected using alumina wedges, which flatten the field and allow the illumination of an array of cameras with parallel optical axes as described in Section 5.

Table 1. Polynomial Coefficients ($A_{i,j}$) Describing the Three Freeform Mirrors (M1, M2, M3 for Primary, Secondary and Tertiary) Surfaces in Their Local Coordinate System, which Is Centered on Each Mirror (See Table 2)[a]

	$A_{0,1}$	$A_{2,0}$	$A_{0,2}$	$A_{2,1}$	$A_{0,3}$	$A_{4,0}$	$A_{2,2}$	$A_{0,4}$	$A_{4,1}$	$A_{2,3}$	$A_{0,5}$
M1	−4.9656	−140.8171	−116.1019	5.6312	4.1057	0.2358	0.0935	−0.1069	—	—	—
M2	−17.6056	−403.0607	−230.5055	61.6645	25.4229	11.6971	−2.4272	−3.5109	—	—	—
M3	−22.1905	−330.6599	−280.4026	28.1685	17.4860	−2.1208	−10.8356	−5.7779	0.8436	1.9139	0.6830

[a]These coefficients are used with Eq. (1) to fully describe the telescope mirror surfaces. Units are mm; coefficients shown with a dash are zero.

Table 2. Positions and Rotation Angles Describing the Local Coordinate Systems of the Three Mirror Surfaces (M1, M2 and M3) and the Focal Plane (FP)[a]

Surface	X [mm]	Y [mm]	Z [mm]	α [deg]
M1	0.0	0.0	0.0	155.40
M2	0.0	5615.0	4898.0	171.16
M3	0.0	8367.0	445.0	−170.88
FP	0.0	9575.8	5024.4	168.93

[a]Origin of coordinates lies at the center of the primary mirror M1, z-axis points towards the boresight and the x-axis points into the page. Rotations shown are with respect to the x-axis and follow the right-hand convention (clockwise is positive).

3. TELESCOPE NOMINAL PERFORMANCE

Image quality for the three-mirror telescope was quantified using Zemax OpticStudio at $\lambda = 1.1$ mm in the time-forward direction (sky → mirrors → focal plane) using a circular aperture of 5 m perpendicular to the boresight. The telescope yields Strehl ratios above 0.94 over 1.1 m or 4.7° in semi-diameter. Figure 2 (bottom) shows Strehl ratios over the unvignetted field of view. Figure 3 shows simulated Huygens diffraction beams and spot diagrams for this system.

We quantify f-numbers by tracing rays in the time-forward direction and computing the angle formed by the chief ray and the marginal ray in four directions at the focal plane. We compute the f-number according to $f/\# = 1/2 \tan(\theta)$. Figure 4
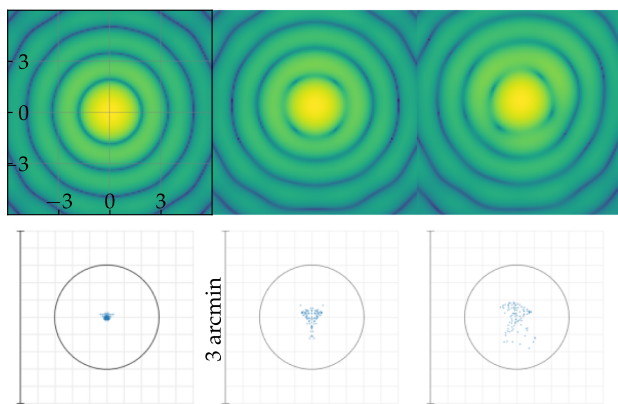

Fig. 3. Three-mirror telescope beam shapes and spot diagrams in sky coordinates (units are arcminutes). Top: monochromatic beam shapes at $\lambda = 1.1$ mm computed with a Huygens diffraction model (Zemax) using uniform illumination of the stop and an aperture of 5 m in the time-forward direction. Bottom: corresponding spot diagram for the center and two extreme field positions 4.7° from the boresight. Field positions in the focal plane are (from left to right) (0, 0) mm, (0, 1100) mm and (1100, 0) mm. All rays lie within an Airy disk radius given by $1.22\frac{\lambda}{D}$ for a wavelength of 1.1 mm and a diameter of 5 m. Strehl ratios for these three fields are 0.99, 0.97 and 0.95.
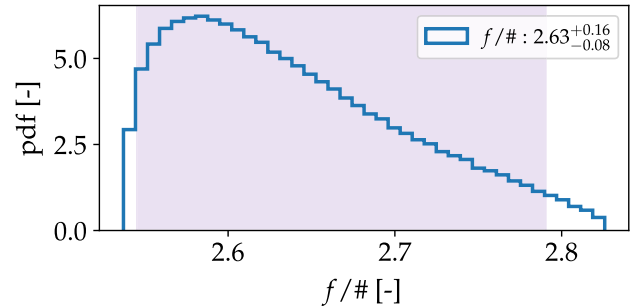

Fig. 4. Chief ray-relative average f-number for the three-mirror telescope across the x-y directions. Label denotes the median f-number with 95% limits across all fields in the sky.

shows a histogram of the chief ray-relative f-number, which has a median value of 2.63. As shown in Fig. 2 (top) and discussed in Section 2, the focal surface is moderately curved. The angle between the chief ray and the focal surface in this design stays between zero and 8°. This level of field curvature can be corrected using a wedge (with a unique tilt and clocking for each camera) as discussed in Section 5. The cone of light reaching the focal plane (for a circular stop in front of the primary mirror) is circular (to within 1%) at the center of the field of view and has a varying ellipticity across the focal plane, with a maximum ellipticity of 9% at the bottom.

4. TELESCOPE TOLERANCES

Tolerance analysis of a freeform system is complex due to the many non-orthogonal parameters that define the optical surfaces and the correlations among them. In addition, the presence of gravitational and thermal deformations further complicates the analysis. To simplify the tolerance analysis of the three-mirror telescope, we split it as follows: (1) first we compute a classical tolerance analysis, where we vary the positions and tilts for the three mirrors in the system one by one and jointly in a Monte Carlo simulation (with and without refocusing) and (2) we implement gravitational and thermal deformations obtained from a computational finite element analysis model to estimate the degradation in image quality due to the deformation of the mirrors.

A. Tolerancing in Mirror Placement and Tilts

We use a three-mirror telescope time-forward model, where we vary the distances between mirrors (three variables), tilts (six variables) and mirror decenterings (six variables). We define a merit function as the minimum Strehl ratio at eight positions located 4.7° from the boresight. The minimum Strehl ratio is

Table 3.   Tolerances for the LAT Telescope without Cameras[a]

Parameter	Tol.	Tol. MC	Tol. Ref.	Tol. Ref. MC
Mirror dist. [mm]	5	2	14	6
Decenter [mm]	5	2	5	2
Tilt [deg]	0.09	0.03	0.09	0.03

[a]Tolerances for single parameter variations produce a degradation in Strehl of 5%. Single parameter tolerances are shown without refocusing (column Tol.) and with refocusing (column Tol. Ref.). Tighter parameters are obtained with a joint Monte Carlo model, where all parameters are randomly varied following a normal distribution. Monte Carlo runs are shown without refocusing and with refocusing (Tol. MC and Tol. Ref. MC, respectively). Note that a 0.03° tilt in a 5-m mirror yields a 2.7-mm peak-to-peak surface error.

used to avoid averaging over a large area with a uniform Strehl ratio, which biases the average high. This metric is more stringent than simply taking the average Strehl ratio. We find values for these 15 variables that degrade this merit function by 0.05. This degradation is found by varying these 15 parameters one at a time, while keeping the rest of the parameters in their nominal values. We find that for this criterion, an inter-mirror distance variation of $\pm 5\,\text{mm}$, a mirror decentering of $\pm 5\,\text{mm}$ and $\pm 0.09°$ of tilt results in a 5% degradation without refocusing compensation. Refocusing compensation allows a relaxation in the tolerance for mirror placement to $\pm 14\,\text{mm}$ while keeping the tolerances in decentering and tilts unmodified. These values are summarized in Table 3, where columns labeled *Tol.* and *Tol. Ref.* show the single variable tolerances without and with refocusing compensation, respectively.

In a Monte Carlo simulation we jointly vary the 15 variables reducing the maximum allowable variation found in the previous paragraph. The maximum allowable variation is obtained by scaling the individual variation by a factor of $1/2.4$. This keeps the Strehl ratio degradation approximately in the same scale as our 5% limit under assumption of uncorrelated random variations (assuming independence and linearity, the merit function scales approximately with $1/\sqrt{15}$). We find that a degradation of less than 5% in the merit function happens 99% of the time for tolerances better than 2 mm in inter-mirror distances, 2 mm in decenters and 0.03° in mirror tilts. Refocusing improves the tolerance in mirror distances to 6 mm, while keeping the decenter and tilt tolerances unmodified. The result of this Monte Carlo simulation can be interpreted as the worst case due to the unexplored correlations among variables, which are expected to reduce independence among the random variables in the simulation.

B. Gravitational Deformation

Gravitational deformations are predicted using a finite element analysis model of the primary and tertiary mirrors. This mechanical model includes the mirror's backing structure with the appropriate support mounting points. The deformation for this surface shows a peak next to a valley in the y direction with a root-mean-square (RMS) value of 10 µm for the primary and 20 µm for the tertiary. We model the secondary with a scaled down version of the deformations of the primary in the opposite direction because the secondary is convex.

We fit a polynomial $f(x, y)$ to the deformation surface in the same format as Eq. (1). This polynomial form is convenient for optical modeling as the perturbed mirror shape can be found by straightforward addition. We find that a polynomial of fifth degree adequately fits this surface with a residual RMS lower than 3 µm for the primary mirror. This three-mirror deformation results in a displacement of the telescope focal point by 1.4 mm away from the tertiary mirror, decreasing the lowest Strehl ratio (which corresponds to the top side of the focal plane) by 2%, i.e., to 0.94.

C. Thermal Deformation

A thermal model of the primary mirror is used to estimate the cupping due to the differential thermal contraction between the mirror backing structure and the optical side of the mirror. We obtain a sag of 60 µm for the primary mirror. We scale the sag of the primary mirror with the diameter of the secondary and tertiary mirrors to estimate their sag assuming a linear relation with mirror diameter to obtain sags of 39 and 60 µm, respectively. We convert the sag of the perturbation to a radius of curvature using the equation

$$R = \frac{r^2 + \delta z^2}{2\delta z}, \tag{2}$$

where R is the radius of curvature of the perturbing surface, r is the radius of the mirror aperture and δz is the sag of the perturbation obtaining radii of curvature of 5.33×10^7 mm for the primary and tertiary and 3.50×10^7 mm for the secondary mirror. This deformation moves the focal plane forward (towards the tertiary) 9.7 mm, which can be refocused obtaining similar performance to the unperturbed case.

D. Thermal + Gravitational Deformation

We combine the thermal and gravitational deformation mentioned above and refocus the system. The new focal point is located 10.24 mm away from the unperturbed focal surface; we find that the minimum Strehl for this configuration is 0.92, while the maximum Strehl ratio stays at 0.99, showing that the combined deformation only degrades the minimum Strehl ratio by roughly 4% if refocusing is allowed. Table 4 shows a summary of the nominal, thermal and gravitational deformation Strehl ratios and their refocus amplitude.

5. CAMERA DESIGN

The receiver consists of an array of 85 three-lens cameras arranged in a hexagonal lattice following center positions (x, y) given by

Table 4.   Telescope Strehl Ratio Variations Due to Mirror Deformations[a]

Deformation	Min Strehl [-]	Max Strehl [-]	Defocus [mm]
Nominal	0.96	0.99	0
Thermal	0.96	0.99	−9.69
Gravity	0.94	0.99	−1.36
Thermal + Grav.	0.92	0.99	−10.24

[a]The image quality at the center field stays without variation, while the mirror shape distortions degrade the top field image quality by 4%.
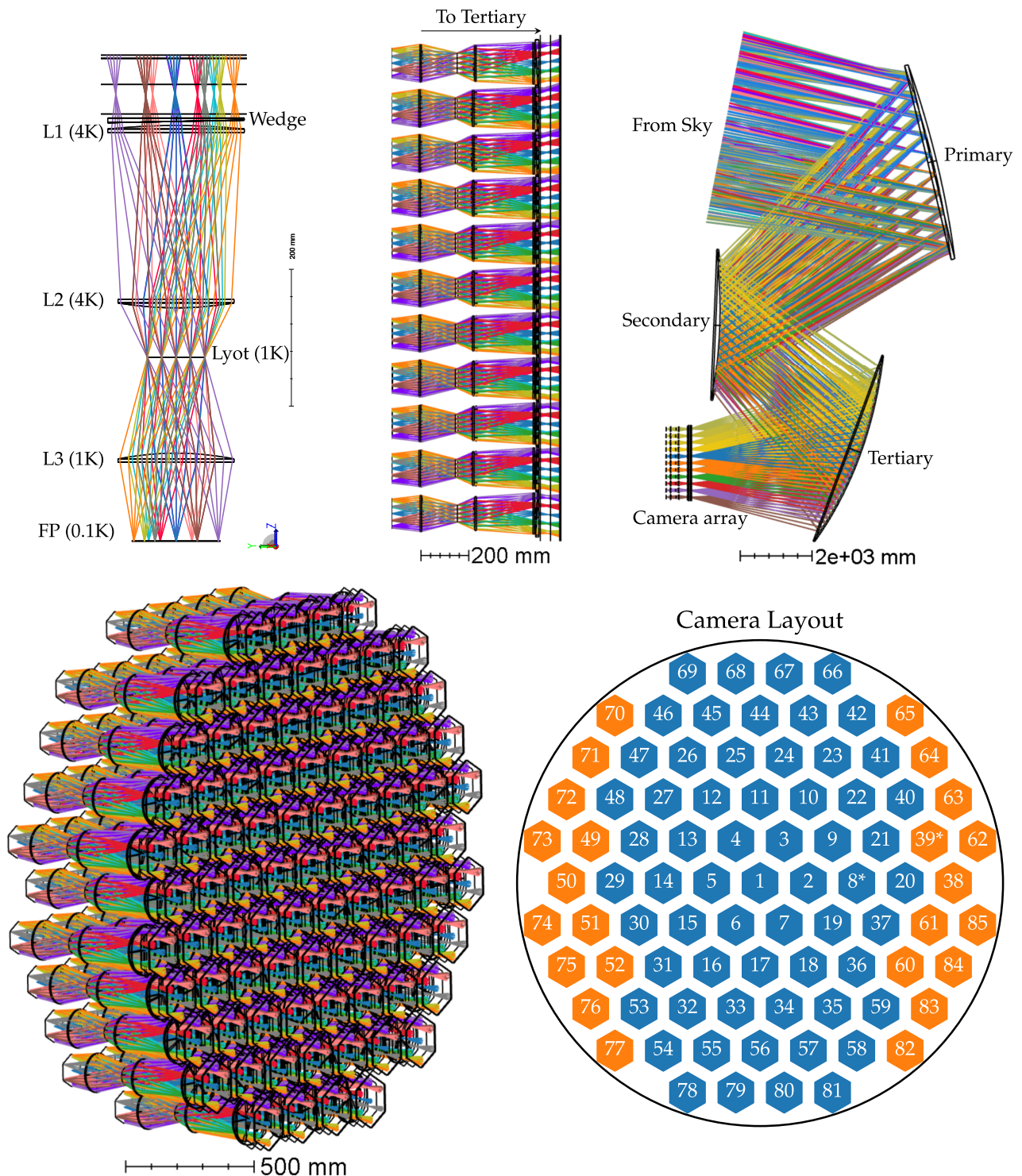
Fig. 5. Top left: optical layout for one of the 85 cameras (camera labeled 1) in the array, three silicon lenses named L1, L2, L3 (from top to bottom) and a Lyot stop are shown. An alumna wedge is placed in front of L1. Top center: side view of the 85 cameras and their wedges. Top right: side view of the three-mirror telescope with its 85 cameras. Bottom left: 85 camera array layout. Bottom right: camera arrangement and numbering convention used in this design. Cameras 8 and 39 have been optimized with the procedure described in Section 5. Circle has a radius of 1100 mm.

$$
\begin{bmatrix} x \\ y \end{bmatrix} = s \begin{bmatrix} \sqrt{3} & \frac{\sqrt{3}}{2} \\ 0 & \frac{3}{2} \end{bmatrix} \begin{bmatrix} a \\ b \end{bmatrix}, \tag{3}
$$

where $s = 219/\sqrt{3}$ mm is a scale parameter and a, b are integer indices. Lenses in each camera are named L1, L2, L3 (ordered

from telescope focal plane towards camera focal plane). A Lyot stop is placed between L2 and L3, which defines the primary mirror illumination. Cameras have parallel axes and the first lens of all cameras (L1) is placed with its vertex located in the same plane.
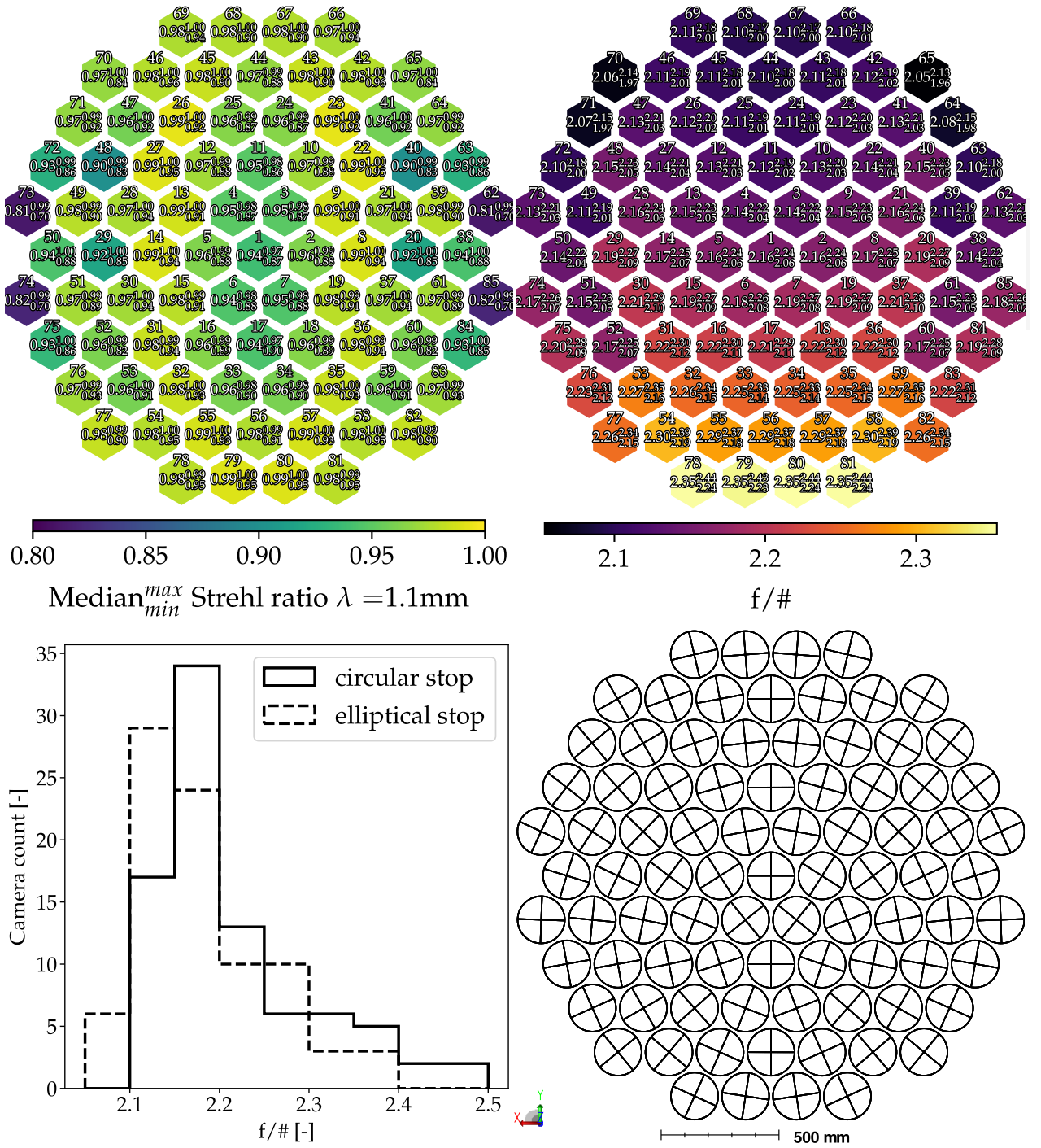
Fig. 6. Top left: median, minimum and maximum Strehl ratios for each of the 85 cameras at $\lambda = 1.1$ mm. Top right: f-number distribution across 85 cameras. Superscript (subscript) denotes the maximum (minimum) f-number value in a particular camera. Bottom left: histogram showing the average f-number distribution for all 85 cameras. Bottom right: alumina wedge clocking for all cameras. Cross is shown as a comparison against the un-rotated x-y axes. Tilt angle and rotation were found optimizing to keep the footprint on the primary within a constant 150 mm from the edge of the mirror.

All lenses are radially symmetric plano–convex, with the shape of the curved side given by

$$z = \frac{c\,r^2}{1 + \sqrt{1 - (1+k)c^2 r^2}}, \qquad (4)$$

where c is the inverse of the radius of curvature R, k is the conic constant and linear units are mm. Field curvature from the telescope is corrected by an alumina wedge with a tilt and clocking that is found numerically in the time-reverse sense to center the footprint envelope for each camera on the primary mirror and to

leave a clearance of 150 mm from the primary rim, which helps shield against spillover.

Optimization of the cameras is performed in the time-reverse sense, with light rays starting at the focal plane of detectors (which has a diameter of 130 mm) passing through the three lenses and mirrors towards the sky. This time-reversed model allows a simple pupil definition, which directly controls illumination of the primary mirror. Optimization is started with approximate shapes for the three lenses (see [14] for more detail on the initial parameters) and the alumina wedge (which can be approximately obtained by pointing the chief ray towards the center of the primary), while keeping a fixed diameter for the Lyot stop of 43 mm, which was found to provide a camera length of about 600 mm and provides reasonable lens curvature. A merit function is defined such that it minimizes the RMS spot-diameter size on the sky for fields distributed across the camera focal plane (see [14] for more details). We also include constraints that keep all rays within the diameter of the lenses and constraints that make a circular stop fully illuminated. The primary illumination is controlled approximately by sampling the marginal rays in the x direction to roughly fill the primary. We optimize cameras over 10 variables (six variables controlling the shapes of the lenses according to Eq. (4) and four variables controlling their spacings). We optimize all 85 cameras individually and evaluate each camera to find if a solution can be successfully replicated to minimize manufacturing complexity. We find that two solutions for the shapes and distances of the lenses are enough to give an acceptable Strehl ratio across the field of view of the telescope. These two solutions cover: (1) the center region (61 cameras) of the array of cameras and (2) the two areas at the sides of the array (composed of 24 cameras) as shown in Fig. 5 (bottom right), where blue and orange denote the two blocks of cameras sharing the same prescription. Values for these two groups of cameras are shown in Table 5.

After finding the optimum values for the lens shapes and distances, the stop size is adjusted for each camera by tracing a ring of marginal rays onto the primary mirror and calculating the distance between this ring of rays and the mirror rim. The stop size is found by making this distance equal to 150 mm (which effectively uses part of the primary to control spilled power) while keeping the center of mass for this ring of rays centered at the primary origin. We do this for a circular stop over three variables (the stop size, camera wedge tilt and clocking angle), and an elliptical stop over five variables (stop semiaxes and clocking, camera wedge tilt and wedge clocking angle). We evaluate the f-number as described in Section 6 and conclude that between these two candidate designs the elliptical stop gives better primary mirror illumination and lower f-numbers as shown in Fig. 6 (bottom left).

Table 5. Parameters Found with the Optimization Procedure Described in Section 5[a]

R_1	R_2	R_3	k_1	k_2	k_3	th_1	th_2	th_3	th_4
−432.8	467.4	−899.4	−9.9	−7.9	−10.7	120.0	143.4	67.3	236.4
−422.9	458.3	−923.6	−10.3	−8.0	−9.9	120.6	139.3	66.4	246.0

[a]Distances between L1-L2, L2-Stop, Stop-L3 and L3-FP are denoted with th_1, th_2, th_3, th_4. All distances and radii of curvature R_j have units of mm.

6. CAMERA PERFORMANCE

Strehl ratios for all 85 cameras are evaluated using the nominal design found in the previous section. Figure 7 (top) shows Strehl ratios for cameras 1, 31 and 83. Figure 6 (top left) shows that 81 cameras are completely diffraction-limited (Strehl ratio greater than 0.8 across the full array) at $\lambda = 1.1$ mm. At $\lambda = 2$ mm, all 85 cameras reach the diffraction limit.

We evaluate f-numbers at the focal plane for the full system consisting of the 85 cameras with their elliptical stops. The f-number is computed in the time-reverse sense by tracing a cone of marginal rays from the detector focal plane onto L3, to the stop and finally to a screen that is placed at a large distance from the stop. The solid angle covered by the marginal ray cone is computed fitting an ellipse to the curve drawn by the marginal rays at this far screen. The f-number is computed as $f/\# = \frac{1}{2\tan\theta}$, where θ is obtained as the geometric mean of the semiaxes of this best-fit angular ellipse (the geometric mean preserves the solid angle of the cone as $\Omega = \pi(\sqrt{ab})^2 = \pi\theta^2$). Figure 7 (bottom) shows f-numbers for cameras 1, 31 and 83. The f-numbers evaluated over the 85 cameras are shown in Fig. 6 (top right). Figure 6 (bottom left) shows histograms of f-numbers for a circular stop, demonstrating that elliptical stops achieve a lower f-number than circular stops. Optomechanical design work is under way to determine filter placement from a cryogenical perspective; we leave its impact on f-number as future work.

Figure 8 shows beams and ellipticities for three cameras: 1, 31 and 83, with histograms for ellipticities obtained from a Huygens diffraction point spread function model. We evaluate the field of view of each camera by tracing the chief ray from the focal plane to the sky for two extreme focal plane positions in the y direction (−61 mm and +61 mm) corresponding to opposite tips of the hexagon. We compute the dot product of the direction vectors for these two rays. We obtain a per-camera median full field of view of 0.68°, a maximum of 0.71° and a minimum of 0.64° across all cameras.

Telecentricity is evaluated by tracing the chief ray through the system and measuring the angle from the normal for all points in the focal plane. With this procedure we confirm all telecentric angles are lower than 2.5°, which is imposed as a hard limit during optimization.

Cross polarization is evaluated for the camera and telescope by inserting orthogonal polarizing grids at the detectors and in
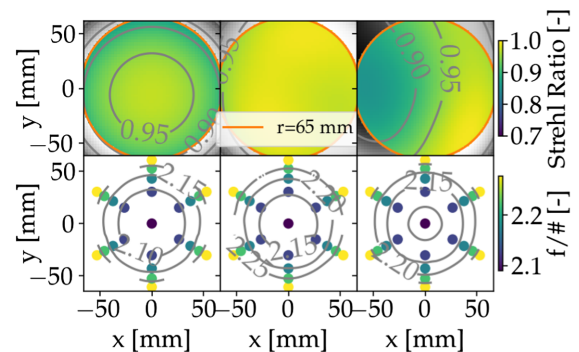

Fig. 7. Strehl ratios at $\lambda = 1.1$ mm (top) and f-numbers (bottom) for cameras 1, 31 and 83 (from left to right). Axes show positions at the detector focal plane.
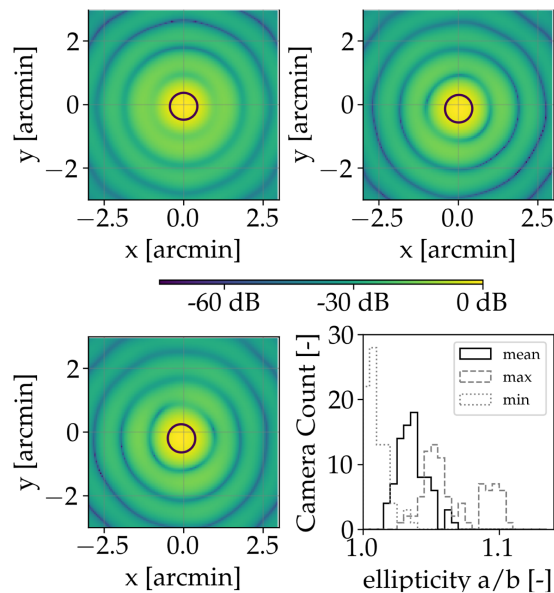
Fig. 8. Upper left, upper right and bottom left: simulated Huygens diffraction beams for cameras 1, 31 and 83, respectively, for an extreme field located 61 mm from the center of the focal plane in the vertical direction. Bottom right: histograms showing the mean, minimum and maximum ellipticity for all 85 cameras.
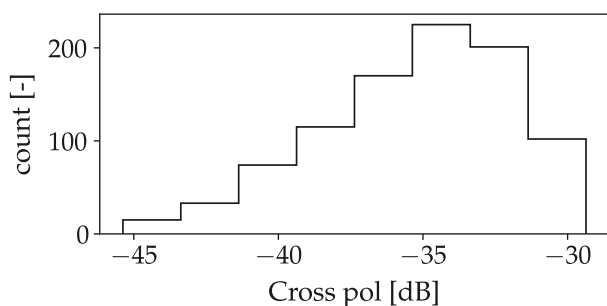

Fig. 9. Cross-polarization across the focal plane for the 85 cameras.

the far field of the telescope. This is evaluated in 11 fields for the 85 cameras, and results are shown in the histogram in Fig. 9. We obtain cross-polarization lower than -29.4 dB in the ray tracing limit.

The point spread function (PSF) is calculated using an electromagnetic simulation software provided by Ticra-Tools (formerly GRASP), in which surface currents on a reflector are computed when the reflector is both being illuminated by a field and radiating in the surrounding space. We use a combination of vector Physical Optics calculations to compute the fields produced by the mirrors and Method of Moments to compute fields produced by the camera. Physical Optics is a sequential simulation that allows computation of incident and reflected fields on a reflector using an appropriate discretization of the reflector surface and its boundary conditions. Method of Moments (MoM) is a full-wave solution of Maxwell equations, which includes internal reflection effects and allows for the application of anti-reflective coatings on refractive surfaces. MoM is used to simulate the three lenses and the wedge within one camera. In this simulation the field is propagated in the time-reverse direction starting from one pixel of the camera 1 focal plane; we
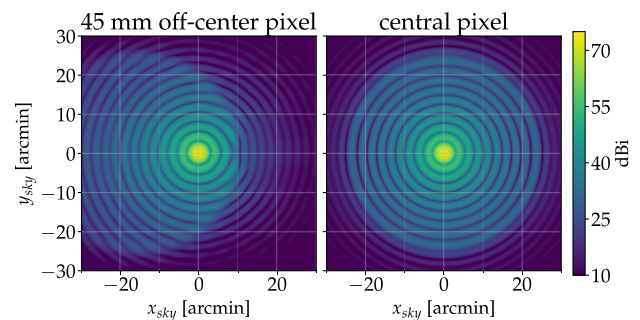

Fig. 10. Monochromatic far-field beam shape at 90 GHz obtained with Ticra-Tools (formerly GRASP) by a combination of Physical Optics (for mirrors and stop) and full-wave Method of Moments (for lenses and wedges) in time-reverse direction. Illumination is set with a Gaussian beam taper of -3 dB at 18°. Left panel shows one pixel 45 mm from the center of the detector focal plane, and the right panel shows the central pixel.

simulate the central pixel and an off-axis pixel located 45 mm off-center. The beam pattern of one horn at the detector focal plane is simulated with a Gaussian profile, tapered 3 dB down the peak at 18.1° from its boresight, as indicated by an early horn beam model. An additional stop is placed at the exit of lens 1 (L1) to model radiation absorbed and scattered by the interior of the cryostat (not included in this sequential analysis). The field at the window towards the tertiary mirror is normalized to have a total irradiated power of 4π Watts, which gives the beam gain in dBi units. Nominal power spilling past the primary mirror is calculated under 0.5% for a wedge reflectance of 20 dB for the central pixel. A cross polarization lower than 45 dB is obtained relative to the copolar component. The far field beam shapes at 90 GHz for the 45-mm off-axis pixel (left) and center pixel (right) are shown in Fig. 10.

7. TELESCOPE–CAMERA TOLERANCES

A. Camera

Camera tolerances are obtained with the telescope at its nominal configuration and perturbing the distances between lenses and Lyot stop (four variables), the lens centering (three variables) and lens tilts (six variables). We define a merit function in camera number 8, which computes the average Sterhl ratio in 25 fields. We perturb each variable while keeping the rest at their nominal value, and we search for a 5% degradation in average Strehl. Figure 13 (two top rows) shows the average Strehl metric as a function of a single variable perturbation in the nominal design. Single variable tolerances are in the 5-mm range and allowable tilts are in the 4° range using this criterion. Multivariable Monte Carlo analysis returns a joint allowable tolerance of 1.5 mm in lens distances and 3.5 mm in lens decenterings, with a 1.5° tolerance in lens tilt. Table 6 shows a summary of this tolerancing analysis and Fig. 13 (bottom panel) shows a histogram of average Strehl ratios for independent and uncorrelated Monte Carlo realizations using these values.

Table 6. Tolerancing for Camera 8[a]

Tolerance Type	Single Par.	Joint MC
Distance [mm]	5	1.5
Decenter [mm]	6	3.5
Tilt [deg]	4	1.5

[a]Single parameter values (column single par.) obtained for a degradation of 0.05 in average Strehl ratio across the 120-mm focal plane. Joint Monte Carlo results in the same degradation varying all variables independently.

B. Telescope–Camera tolerance

We extend the model presented above to include variations to the three mirrors and the camera refractive optical elements. Random and independent realizations of this system with amplitudes of 1.5 mm for the distances between optical elements, 1.0 mm for the de-centering of all optical elements, tilts of 0.5° for all lenses plus alumina wedge and 0.03° for the three mirrors result in that more than 90% of realizations introduce a degradation in the minimum Strehl ratio in the detector focal plane of less than 0.04. Refocusing will relax these tolerances. We leave a more detailed tolerancing study, including FEA deformations, for future studies.

C. Deformed mirrors

We evaluate Strehl ratios with the three deformed mirrors. We include thermal warping and gravitational deformations as described in Section 3.A; we also allow the camera to vary position to refocus. We obtain acceptable image quality as characterized by Strehl ratio coverage. In particular, we find that 81 cameras have diffraction-limited image quality (Strehl ratio > 0.8) at $\lambda = 1.1$ mm as shown in Fig. 11 (left), and at $\lambda = 2$ mm we find that diffraction-limited performance is achieved in all 85 cameras as shown in Fig. 11 (right).

8. CONCLUSION

We have presented a freeform three-mirror anastigmatic large-aperture telescope, capable of observing a wide 9.4° field of view at $\lambda = 1.1$ mm. A detailed description of this design is given accompanied by a suite of metrics that indicate excellent performance. We have also presented a detailed description of an array of 85 cameras that can observe up to $\lambda = 1.1$ mm in wavelength with diffraction-limited performance in 81 of 85 cameras and with all 85 cameras at 2 mm. We have shown expected performance and tolerancing. We continue to iterate on the opto-mechanical design of the telescope and cameras, including detailed thermal and mechanical effects in order to prepare this design for manufacture.

APPENDIX A: TELESCOPE AND CAMERA TOLERANCING

In Sections 4 and 7 we describe the merit function used to compute tolerancing metrics. Figures 12 and 13 show the merit function variation under single camera variations for displacement variables (top panel), angular tilt variables (center panel) and a histogram of Monte Carlo realizations for the case of the telescope alone (Fig. 12) and the three-mirror telescope system with camera 8 (Fig. 13).
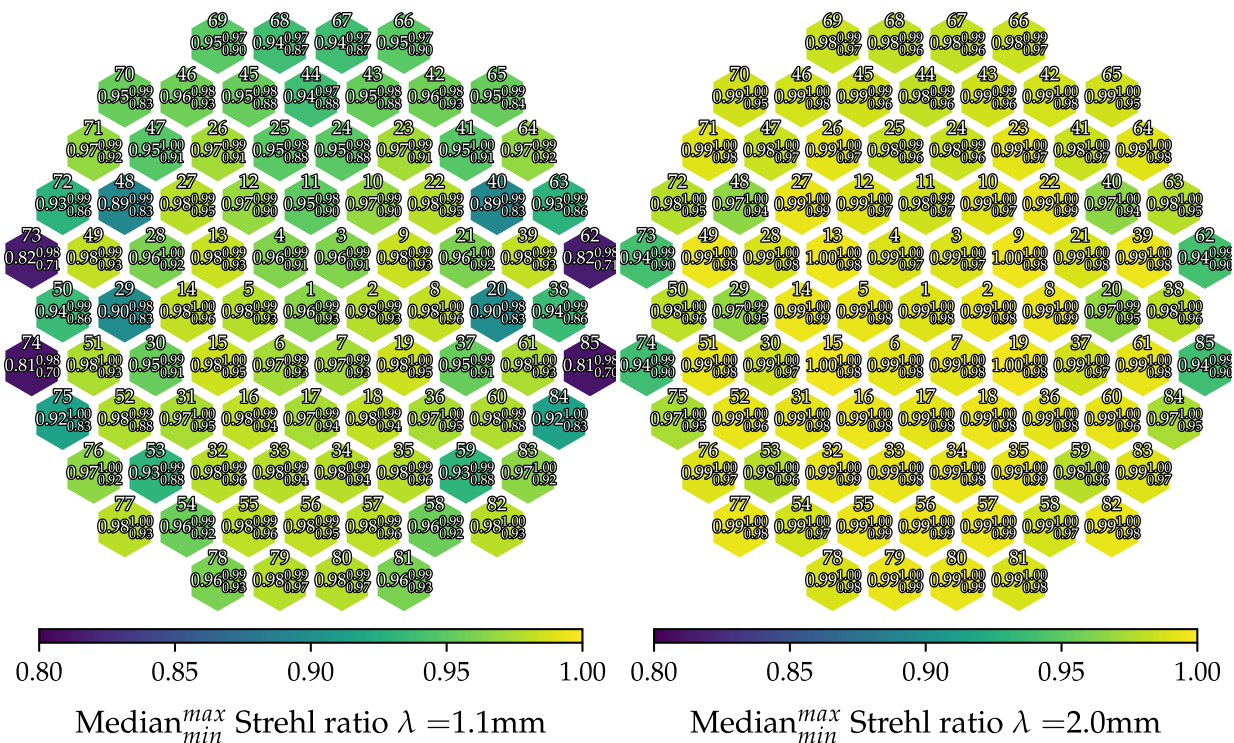

Fig. 11. Left: Strehl ratios at $\lambda = 1.1$ mm for the 85-camera design presented in Section 4.A with mirror gravitational and thermal deformations described in Section 5.A. Right: the same system evaluated at 2 mm shows that all cameras show diffraction-limited performance (above 0.8).
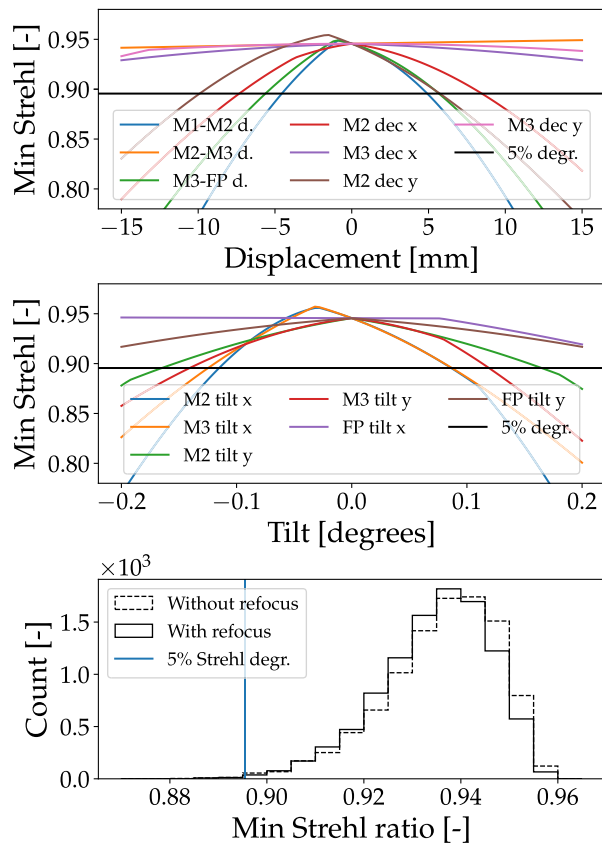
Fig. 12. Tolerancing of the telescope three-mirror system without reimaging camera optics. Top: single parameter variations in the minimum Strehl ratio evaluated at the edge of the focal plane 4.6° from the boresight. Center: single parameter variations for the tilt parameters of the minimum Strehl ratio. Bottom: Monte Carlo tolerancing simulation of the three-mirror telescope presented in this work. Histogram describes the Strehl ratio variation, during random changes to mirror misplacement and tilts as described in Section 4.A and for parameters shown in Table 3.
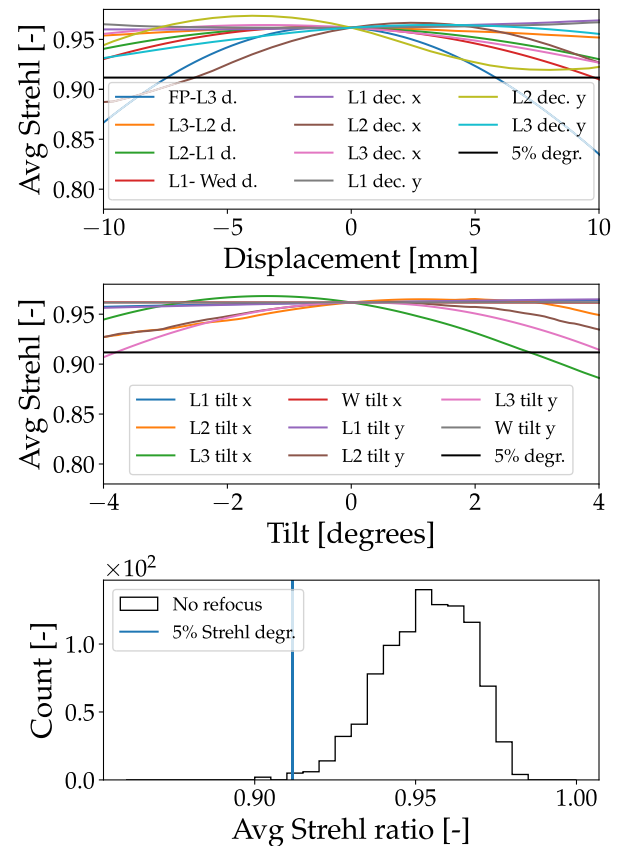

Fig. 13. Single variable tolerancing for camera 8. Top: average Strehl ratio for a perturbation in lens distances and decenter. Center: average Strehl for a perturbation in lens tilts. Bottom: Monte Carlo sampled average Strehl ratios for the values in Table 6.

Data availability. The optical design presented here can be reproduced using the tables in this document.

REFERENCES

1. K. N. Abazajian, P. Adshead, Z. Ahmed, *et al.*, *Cmb-s4 Science Book*, 1st ed. (2016).
2. K. Abazajian, G. Addison, P. Adshead, *et al.*, "CMB-S4 science case, reference design, and project plan," arXiv, arXiv:1907.04473 (2019).
3. J. W. Fowler, M. D. Niemack, S. R. Dicker, *et al.*, "Optical design of the Atacama Cosmology Telescope and the millimeter bolometric array camera," Appl. Opt. **46**, 3444–3454 (2007).
4. S. Padin, Z. Staniszewski, R. Keisler, *et al.*, "South pole telescope optics," Appl. Opt. **47**, 4418–4428 (2008).
5. S. C. Parshley, M. Niemack, R. Hills, S. R. Dicker, R. Dünner, J. Erler, P. A. Gallardo, J. E. Gudmundsson, T. Herter, B. J. Koopman, M. Limon, F. T. Matsuda, P. Mauskopf, D. A. Riechers, G. J. Stacey, and E. M. Vavagiakis, "The optical design of the six-meter CCAT-prime and Simons Observatory telescopes," Proc. SPIE **10700**, 1070041 (2018).
6. C. Dragone, "A first-order treatment of aberrations in Cassegrainian and Gregorian antennas," IEEE Trans. Antennas Propag. **30**, 331–339 (1982).
7. Y. Mizuguchi, M. Akagawa, and H. Yokoi, "Offset Gregorian antenna," Electron. Commun. Jpn. **61**, 58–66 (1978).
8. C. Dragone, "First-order correction of aberrations in Cassegrainian and Gregorian antennas," IEEE Trans. Antennas Propag. **31**, 764–775 (1983).
9. J. W. Contreras and P. A. Lightsey, "Optical design and analysis of the James Webb Space Telescope: optical telescope element," Proc. SPIE **5524**, 30–41 (2004).
10. Ž. Ivezić, S. M. Kahn, J. A. Tyson, *et al.*, "LSST: from science drivers to reference design and anticipated data products," Astrophys. J. **873**, 111 (2019).

11. R. Gilmozzi and J. Spyromilio, "The European extremely large telescope (E-ELT)," Messenger **127**, 11 (2007).

12. A. Laborie, R. Davancens, P. Pouny, C. Vétel, F. Chassat, P. Charvet, P. Garé, and G. Sarri, "The Gaia focal plane," Proc. SPIE **6690**, 66900A (2007).

13. S. Padin, "Three-mirror anastigmat for cosmic microwave background observations," Appl. Opt. **57**, 2314 (2018).

14. P. A. Gallardo, B. Benson, J. Carlstrom, S. R. Dicker, N. Emerson, J. E. Gudmundsson, R. Hills, M. Limon, J. McMahon, M. D. Niemack, J. M. Nagy, S. Padin, J. Ruhl, and S. M. Simon, "Optical design concept of the CMB-S4 large-aperture telescopes and cameras," Proc. SPIE **12190**, 121900C (2022).

15. I. Gullett, B. Benson, R. Besuner, R. Bihary, J. Carlstrom, N. Emerson, P. A. Gallardo, J. Gomez, C. L. King, J. McMahon, J. L. May, J. M. Nagy, T. Natoli, M. D. Niemack, K. Okun, S. Padin, J. E. Ruhl, E. J. Wollack, and J. Zivick, "Sidelobe modeling and mitigation for a three mirror anastigmat cosmic microwave background telescope," Appl. Opt. **62**, 4334–4341 (2023).

16. T. Natoli, B. Benson, J. Carlstrom, E. Chauvin, B. Clavel, N. Emerson, P. Gallardo, M. Niemack, S. Padin, K. Schwab, L. Stenvers, and J. Zivick, "Fabrication of a monolithic 5 m aluminum reflector for millimeter-wavelength observations of the cosmic microwave background," Appl. Opt. **62**, 4747–4752 (2023).

17. R. J. Thornton, P. A. R. Ade, S. Aiola, *et al.*, "The Atacama Cosmology Telescope: the polarization-sensitive ACTPol Instrument," Astrophys. J. Suppl. Ser. **227**, 21 (2016).

18. P. A. Gallardo, J. Gudmundsson, B. J. Koopman, *et al.*, "Systematic uncertainties in the Simons Observatory: optical effects and sensitivity considerations," Proc. SPIE **10708**, 658–673 (2018).

19. S. R. Dicker, P. A. Gallardo, J. E. Gudmundsson, *et al.*, "Cold optical design for the large aperture Simons' Observatory telescope," Proc. SPIE **10700**, 107003E (2018).

20. J. E. Gudmundsson, P. A. Gallardo, R. Puddu, *et al.*, "The Simons Observatory: modeling optical systematics in the Large Aperture Telescope," Appl. Opt. **60**, 823 (2021).

21. J. Ruhl, P. A. R. Ade, J. E. Carlstrom, *et al.*, "The South Pole Telescope," Proc. SPIE **5498**, 11–29 (2004).

22. J. E. Carlstrom, P. A. R. Ade, K. A. Aird, *et al.*, "The 10 meter south pole telescope," Publ. Astron. Soc. Pac. **123**, 568 (2011).

23. S. W. Henderson, R. Allison, J. Austermann, *et al.*, "Advanced ACTPol cryogenic detector arrays and readout," J. Low Temp. Phys. **184**, 772–779 (2016).

24. E. M. George, P. Ade, K. A. Aird, *et al.*, "Performance and on-sky optical characterization of the SPTpol instrument," Proc. SPIE **8452**, 84521F (2012).

25. J. A. Sobrin, A. J. Anderson, A. N. Bender, *et al.*, "The design and integrated performance of spt-3g," Astrophys. J. Suppl. Ser. **258**, 42 (2022).

26. D. Korsch, "Anastigmatic three-mirror telescope," Appl. Opt. **16**, 2074–2077 (1977).

27. M. S. Longair, "Richard Edwin hills. 30 September 1945-5 June 2022," Biograph. Mem. Fellows R. Soc. **74**, 237–257 (2023).